Title
Liquefaction and Related Ground Failure from July 2019 Ridgecrest Earthquake Sequence

Journal
Bulletin of the Seismological Society of America, 110(4)

ISSN
0037-1106

Authors
Zimmaro, Paolo
Nweke, Chukwuebuka C
Hernandez, Janis L
et al.

Publication Date
2020-08-01

DOI
10.1785/0120200025

Peer reviewed

Liquefaction and Related Ground Failure from July 2019 Ridgecrest Earthquake Sequence

Paolo Zimmaro[1*], Chukwuebuka C. Nweke[1], Janis L. Hernandez[2], Kenneth S. Hudson[1], Martin B. Hudson[3], Sean K. Ahdi[4], Matthew L. Boggs[5], Craig A. Davis[6], Christine A. Goulet[7], Scott J. Brandenberg[1], Kenneth W. Hudnut[8,1], and Jonathan P. Stewart[1]

[1] Dept. of Civil & Environmental Engineering, University of California, Los Angeles, CA

[2] Dept. of Conservation, California Geological Survey, Los Angeles, CA

[3] Turner Engineering Group, Turner Construction Company, Los Angeles, CA

[4] Exponent, Inc.; Dept. of Earth, Planetary, & Space Sciences, Univ. of California, Los Angeles, CA

[5] Naval Air Warfare Center - Weapons Div., US Navy, China Lake, CA

[6] City of Los Angeles Dept. of Water and Power (Retired), Los Angeles, CA

[7] Southern California Earthquake Center, University of Southern California, Los Angeles, CA

[8] U.S. Geological Survey, Pasadena, CA

*Corresponding author: Dept. of Civil & Environmental Engineering, University of California, Los Angeles, 90095 Los Angeles, CA, pzimmaro@ucla.edu

Abstract

The 2019 Ridgecrest earthquake sequence produced a **M**6.4 foreshock on July 4 and a **M**7.1 mainshock on July 5, along with 23 events with magnitude greater than 4.5 in the 24-hour period following the mainshock. The epicenters of the two principal events were located in the Indian Wells Valley, northwest of Searles Valley near the towns of Ridgecrest, Trona, and Argus. This paper describes observed liquefaction manifestations including sand boils, fissures, and lateral spreading features, as well as proximate non-ground failure zones, that resulted from the event sequence. Expanding upon results initially presented in a report of the Geotechnical Extreme Events Reconnaissance Association (GEER), we synthesize results of field mapping, aerial imagery, and inferences of ground deformations from synthetic aperture radar-based damage proxy maps (DPMs). We document incidents of liquefaction, settlement, and lateral spreading in the Naval Air Weapons Station China Lake US military base, and compare locations of these observations to pre- and post-event mapping of liquefaction hazards. We describe liquefaction and ground failure features in Trona and Argus, which produced lateral deformations and impacts on several single-story masonry and wood frame buildings. Detailed maps of zones with and without ground failure are provided for these towns, along with mapped ground deformations along transects. Finally, we describe incidents of massive liquefaction with related ground failures, and proximate areas of similar geologic origin without ground failure in the Searles Lake bed. Observations in this region are consistent with surface change predicted by DPMs. We anticipate that data presented in this paper will be useful for validating near-real time geospatial models and remote-sensing products such as DPMs and for future liquefaction susceptibility, triggering, and consequences studies being undertaken as part of the Next-Generation Liquefaction project.

Introduction

The Ridgecrest earthquake sequence, including the **M**6.4 foreshock on July 4 and the **M**7.1 mainshock on July 5, 2019, occurred on faults formerly considered as part of the greater Little Lake Fault Zone, now differentiated after the recent earthquakes and referred to as the Salt Wells Valley Fault Zone for the **M**6.4 event, and the Paxton Ranch Fault Zone for the **M**7.1 event (Dawson et al., 2020). These are part of the Eastern California Shear Zone (ECSZ), a northward extension of the right-lateral southern San Andreas fault tectonic regime that continues northward through the Owens Valley towards Walker Lane. This zone is bordered to the east by the extensional Basin and Range province. As shown in Figure 1, developed areas locally affected by the sequence include the Naval Air Weapons Station China Lake, the City of Ridgecrest, and the two nearby towns of Trona and Argus in the adjacent Searles Valley. An extensively investigated feature of these events was substantial surface rupture along the causative faults, which is presented by Ponti et al. (2020) and Dawson et al. (2020). In this paper, we describe significant liquefaction-related effects, as well as proximate areas without ground failure, in Searles Valley and Indian Wells Valley.

Following the **M**6.4 event on July 4, 2019, multi-agency reconnaissance teams deployed to the epicentral area to collect perishable information such as ground failure features and related effects on buildings and infrastructure. The information presented in this paper represents composite findings from the following teams deployed in the field at various points in time with different focuses and objectives and utilizing a variety of different reconnaissance tools:

- Geotechnical Extreme Events Reconnaissance (GEER) team (Stewart et al., 2019; Brandenberg et al. 2020b): on-ground mapping and aerial imagery by means of small Uninhabited Aerial Systems (sUAS) focusing on earthquake effects in Trona, Argus, and some portions of the surface fault rupture features (July and August 2019);

- U.S. Geological Survey (USGS) and California Geological Survey (CGS) team: on-ground mapping, helicopter overflights, aerial and ground surface photography focusing on the Naval Air Weapons Station China Lake in Indian Wells Valley (July through September, 2019);
- National Aeronautics and Space Administration (NASA)-supported team: on-ground mapping of ground failure-related damage within the Searles Lake area (November 2019; Zimmaro and Hudson 2019).

The main objectives of this paper are to: (1) document occurrences of liquefaction and adjacent areas of non-ground failure, so as to facilitate the utilization of this data in liquefaction databases (e.g., Brandenberg et al. 2020a; Schmitt et al., 2017); (2) demonstrate the effective utilization of multiple information sources to study liquefaction effects across a broad region with variable access; and (3) use field observations of ground failure to validate spatial data tools including near real-time liquefaction hazard maps produced by USGS and synthetic aperture radar-based damage proxy maps (DPMs) produced by the Advanced Rapid Imaging and Analysis (ARIA) team at the California Institute of Technology (Caltech) and the NASA - Jet Propulsion Laboratory (JPL). All data collected by the GEER- (Brandenberg et al., 2019 and 2020b) and NASA-supported (Zimmaro and Hudson, 2019) teams presented and discussed in this paper are available on DesignSafe (Rathje et al., 2017b). Additional data from the USGS/CGS reconnaissance team, such as aerial and ground-based photos of liquefaction and other water-related ground failure features, which were observed after the **M**6.4 (but before the **M**7.1) as well as after the **M**7.1, are reported in the electronic supplement to this paper

(Table S1 and Figures S1-S16). A few of the ground failure features documented in this paper were also briefly noted by Jibson (2020).

Near real-time damage and liquefaction maps

Damage Proxy Maps

Following major natural and/or anthropogenic events, the ARIA team at Caltech and NASA JPL, produces near real-time maps to identify the extent of potentially damaged areas. These DPMs are produced utilizing Synthetic Aperture Radar (SAR) images. Such techniques are based on differences in phase of radio waves returning to a moving platform. In the case of the DPMs, these platforms are satellites. DPMs are produced by comparing interferometric SAR coherence maps from before and after an extreme event (e.g., Fielding et al. 2005, Yun et al. 2011). Such maps are typically produced following major earthquakes, hurricanes, floods, and wildfires. A known issue with SAR-based data is that damage detection is challenging in areas with potential sources of noise, including vegetation coverage, steep topography, and areas where the landscape is modified over a short period of time (e.g., due to human activities). The study region in Figure 1 contains sparse plant cover. Furthermore, anthropogenic activities only occur in a small portion of this region as it mainly consists of undeveloped land that is publicly inaccessible. As a result, it provides a nearly ideal setting for validating DPM predictions.

DPMs and similar SAR-based products have previously been compared against observations following recent events including the 2011 **M**9.1 Tohoku earthquake (Ishitsuka et al., 2012), the 2015 **M**7.8 Gorkha earthquake (Yun et al., 2015), the 2016

Central Italy earthquake sequence (Franke et al., 2018 and Sextos et al., 2018), and the 2018 **M**6.6 Hokkaido earthquake (Jung and Yun, 2020). These comparisons show good general agreement between areas with building and/or ground failure damage and DPMs. However, additional high-quality observations are needed to develop formal quantitative metrics to analyze the reliability of such maps. As a result, the ground-truth data presented in this paper constitutes a valuable resource to validate DPMs and similar remote sensing products against liquefaction and related ground failure.

A public DPM was released following the Ridgecrest earthquake sequence on July 12 2019 (https://aria-share.jpl.nasa.gov/20190704-0705-Searles_Valley_CA_EQs/DPM/). Figure 1 shows the DPM, observed surface rupture features, and outlines of more detailed maps showing liquefaction features presented in this paper. The DPM in Figure 1 covers an area of 300 by 250 km. Each pixel in the map is 25 by 30 m. This level of resolution can be used to detect regions with high damage. However, it may be too coarse to identify small damage features such as pavement cracks, individual sand boils, or damage to individual buildings. The map was created using SAR data available from the Copernicus Sentinel-1 satellites, operated by the European Space Agency (ESA).

The DPM in Figure 1 is based on pre- and post-event SAR images taken before the **M**6.4 event (on July 4, 2019) and after the **M**7.1 event (on July 10, 2019). During the period between the two image acquisitions, 30 earthquakes with magnitude greater than 4.5 were recorded in the area (USGS, 2020). As a result, damage proxies result from the cumulative effects of multiple events. This map shows colored pixels only where coherence loss values are above the noise threshold (defined by the map developers). These colored pixels represent zones where the map identifies significant surface change (non-zero damage proxies). Pixels with an associated coherence loss lower than the noise threshold are not shown in the map. The map captures well the observed fault surface rupture features from both the **M**6.4 and **M**7.1 events. It also shows extensive surface change within the Searles Lake area and more distributed surface changes in the Paxton Ranch and Salt Wells Valley areas. In the remainder of the paper, we compare observed liquefaction surface manifestations to spatial data tools including DPM predictions in greater detail.

USGS Liquefaction Hazard Maps

As part of the Earthquake Hazards Program, the USGS developed a ground failure earthquake product to augment the Prompt Assessment of Global Earthquakes for Response (PAGER) system (Allstadt et al. 2017). Following major earthquakes worldwide, this product provides near real-time maps of earthquake-induced landslide and liquefaction probabilities. Both the liquefaction and landslide maps are derived from models that utilize ground shaking intensity as an input, which allows the maps to be rapidly generated, but which does not take into account information from remotely sensed images, as the DPMs do.

Geospatial liquefaction models are used to generate the liquefaction hazard maps, which are conditioned on ground motion parameters and globally-available inputs. The two models currently used are:

- Preferred model: Zhu et al. (2017) with additional modifications by Baise and Rashidian (2017)
- Alternate model: Zhu et al. (2015)

Ground motion inputs are taken from ShakeMaps (Wald et al. 2005, Worden and Wald, 2016), which in turn are derived from instrumental recordings, ground motion models, and site conditions estimated from topographic slope (Wald and Allen, 2007). Additional inputs related to liquefaction vulnerability include mean annual precipitation (from Hijmans et al., 2005), distance from the coast (NASA Ocean Color Group; oceancolor.gsfc.nasa.gov/cms/DOCS/DistFromCoast), distance from rivers (from USGS Hydrosheds database; https://hydrosheds.cr.usgs.gov/dataavail.php), and water table depth (from Fan et al., 2013).

The USGS published liquefaction hazard maps following each of the **M**6.4 and **M**7.1 events. Since most of the liquefaction features were observed following the **M**7.1 mainshock, in the remainder of the paper we compare field observations to the second USGS liquefaction hazard map.

Regional Geologic Setting, Geologic Materials, and Geohydrology

Indian Wells Valley and Searles Valley are located in the southwestern corner of the Basin and Range geomorphic province near its interface with the Mojave Desert geomorphic province. The northern portion of the Basin and Range province is called the Great Basin region which is approximately bounded by the Garlock fault on the south and the Sierra Nevada mountains on the west, and extends to the Colorado Plateau to the east and the Columbia Plateau to the north. The province is characterized by interior drainage with lakes and playas, and the typical horst-and-graben geologic structure (subparallel, fault-bounded ranges separated by down-dropped basins) that include valleys such as Death Valley, Owens Valley, and Honey Lake Basin, and associated mountain ranges. The

Mojave Desert geomorphic province is bound by the Garlock fault on the north and the San Andreas fault on the southwest and extends east to the Colorado Plateau. The Mojave Desert province is characterized by a broad interior of isolated mountain ranges separated by desert plains.

Indian Wells Valley and Searles Valley are both alluvial basins characterized by alluvial fan deposits on the flanks of the surrounding mountains with lacustrine deposits in the interior of the basins. The alluvial deposits are derived from the surrounding mountains which are primarily Paleozoic to late Mesozoic granitic bedrock (Kunkel and Chase, 1969) and volcanic deposits (Schweig, 1984).

Indian Wells Valley contains a dry playa called China Lake which is located at an approximate elevation of 650 m above mean sea level (AMSL) (North American Vertical Datum of 1988, NAVD 88). Searles Valley also contains a playa called Searles Lake at an approximate elevation of 490 m AMSL (NAVD 88).

As shown in Figure 2, there are three distinct geologic units within the Indian Wells Valley: alluvium (including some windblown dune deposits), lacustrine deposits, and playa deposits as described by Berenbrock and Martin (1991) and Bullard et al. (2019). The alluvium consists of moderately- to well-sorted gravel, sand, silt, and clay of Pleistocene and Holocene ages and continues to be actively deposited. The fines content increases and the thickness of alluvial deposits decreases toward the central portion of China Lake. Lacustrine deposits contain silt and silty clay of Pleistocene age and overlies the alluvial deposits in the center of the basin (Kunkel and Chase, 1969). Playa deposits consisting of silt and clay with occasional sand lenses overlay the lacustrine deposits are Holocene in age, and are being actively deposited. The aeolian sand dune deposits are Holocene in age (Warner, 1975 and Lancaster et al., 2019).

As shown in Figure 3 (vicinity of Trona and Argus), Searles Valley has a similar stratigraphy to Indian Wells Valley with Pleistocene and Holocene alluvium consisting of fine to coarse sand with little gravel and fines, Holocene playa silt and clay, and Holocene aeolian dune sand. However, the lacustrine deposits differ in that they contain thick evaporite deposits interbedded with lacustrine silts and clays. The evaporites consist primarily of halite, thermonatrite, thenardite, and ulexite with gypsum locally common in some units (Smith, 2009).

The two valleys include two hydrographically closed groundwater basins: Indian Wells Valley and Searles Valley Groundwater Basins of the South Lahontan Hydrologic Region (California Department of Water Resources, DWR, 2003). The Salt Wells Valley Groundwater Basin is located between the two in the saddle where Highway 178 crosses the Argus Range. During the Pleistocene, the region was much wetter and these currently isolated groundwater basins were connected by the Owens River (McGraw et al., 2016).

Based on data from observation wells collected in the period 1959-2019, we reconstructed the depth to ground water in the study area (Figure 1). Within the Indian Wells Valley Groundwater Basin the depth to groundwater varies from the ground surface in the center of the valley near Paxton Ranch to greater than 100 m below ground surface (bgs) on the margins of the valley (California DWR, 2020). Within the Salt Wells Valley Groundwater Basin there is groundwater at the ground surface in the center of the basin to greater than 15 m bgs along the margins (California DWR, 2020). The Searles Valley

Groundwater Basin has surface water present in the central-western portion of the Searles Lake playa associated with mining activity from the Searles Valley Minerals, Inc. Groundwater throughout the playa ranges from less than 1 m bgs to approximately 2 m bgs (California DWR, 2020). The groundwater in this basin is a brine with pH values between 9.2 and 9.5 (Smith, 1979).

Sites at Naval Air Weapons Station China Lake

The Naval Air Weapons Station, China Lake (NAWS) base is located within the Basin and Range geomorphic province of California, within the ECSZ. Developed areas within the NAWS China Lake are primarily within the Indian Wells Valley, located between the Sierra Nevada Mountains to the west, the Coso Range to the north, and the Argus Range to the east. Our observations of liquefaction-related ground failure features in the NAWS were focused primarily within lacustrine and playa deposits.

Reconnaissance Methods

Methods of recording liquefaction features included post-earthquake helicopter overflights and field geologic mapping. High-quality single-lens reflex imagery was used to record observations with GPS-enabled locations, as well as digital photos collected using ArcCollector software on iPad tablets. Both types of imagery were collected in overflight reconnaissance and during field verification. Limits of liquefaction were generally noted during overflight observations. The team performed a subsequent ground deployment targeting surface fault rupture areas. During this field deployment liquefaction features were visited on the ground, when near to surface rupture locations. Due to time constrains with helicopter overflights, available NAWS escorts, and USGS/CGS field teams, our observations focused on primary surface rupture. Overflight reconnaissance was performed at an elevation of about 152 m above the ground surface, or less.

The 3rd and 11th authors comprised the first team members to perform helicopter overflight and aerial photography on the afternoon of July 5, 2019, after the M6.4 foreshock and prior to the M-7.1 mainshock. The next day, helicopter reconnaissance was again performed following the predominantly northwest-oriented surface rupture associated with the July 5, 2019 M7.1 mainshock. Several other overflights were performed on subsequent days. CGS and USGS geologists paired up daily as earthquake response teams, where the primary focus was to document and measure surface rupture and to obtain geo-located photographs of any liquefaction-related or ground failure features. Track logs of these helicopter flights are shown in Figures S17 and S18.

Findings

Review of the distribution of liquefaction-related features was performed by identifying liquefaction features from CGS staff photographs and entering GPS coordinates of each photo into an ESRI ArcGIS geodatabase and map. The GPS coordinates of photos taken during overflights refer to the location of the helicopter. However, we tried, when possible, to identify persistent features on the ground and report the actual location of the observation, rather than the location of the helicopter. As a result, locations of observations made during overflights refer as best as possible to their actual location on the ground. Data were subdivided into separate categories of liquefaction surface manifestations and other ground failure features such as: sand boils, lateral spreading, and seepage or springs. Areas with widespread liquefaction features were then delineated into separate polygons, as shown in Figure 2. At each feature point, hyperlinks were set to link a specific photo file of that feature in our geodatabase currently residing at CGS, which will be made available in the future.

For the NAWS base observations, Table S1 presents locations of liquefaction features observed during post-earthquake reconnaissance, grouped into Areas A-C (North Dry Lakebed Area – Paxton Ranch, Central Area – Southeast end of China Lake, and Southern Area – Salt Wells Valley, respectively). Figures S1-S16 show photos of representative liquefaction effects at selected locations discussed in this section, and listed in Table S1.

As shown in Figure 2, areas of liquefaction-related ground failures from the Ridgecrest earthquake sequence are found within three primary areas on the NAWS base: Paxton Ranch, the southern end of China Lake Playa, and Salt Wells Valley. Site conditions where liquefaction features exist included saturated or very shallow groundwater levels, loose, fine-grained playa and lacustrine sediments, and areas where natural springs occur at bedrock-alluvium contacts. Also, near the southern edge of the China Lake playa, leakage from the sewage ponds and corresponding drainage channels from Lark Seep to the playa are a contributing factor. Seasonal rains collect in both the China Lake and Salt Wells Valley areas, promoting shallow groundwater conditions.

Liquefaction features appeared to coincide with fault surface rupture locations in the Paxton Ranch area. Lateral spreads were prominent throughout the central portion of the small playa in this area and concentrated just inside the outer edges of the playa (Figure 2 and S1). Ground failures that occurred in the Paxton Ranch area did not appear to impact infrastructure, as these features appeared to be fairly constrained to the small, unnamed northern playa surface.

In southern China Lake, springs or seeps were located within the playa deposits, approximately 35-50 m from the bedrock-alluvium contact (35.714920°, -117.592197°). Large sand boils with central openings 2-4 m in diameter were located 125-160 m west of the main **M**7.1 surface rupture (35.733098°, -117.582061°) as shown in Figure 2 and S8. Ground failures were noted in the China Lake area at a sewer treatment pump house, located within the eastern portion of China Lake playa, about 1.7 km west of the main **M**7.1 rupture. Damage to this structure included excavation backfill settlement (ring fractures) and external pipe connection dislocations. Foundation settlement was not observed, although shallow groundwater pumping extended outside the building and some external utility poles were tilted. Lateral spread features were observed along the southern end of China Lake playa near a shallow detention basin (35.723812°, -117.567984°), about 70m away from the bedrock-alluvium contact (Figure S10). Other buildings located along the southern edge of the China Lake playa (35.711727°, -117.601528°) exhibited foundation settlement, displaced or broken water lines, and tilted utility poles.

In the Salt Wells Valley area, lateral spreads were common near channel margins, and along edges of Salt Wells Valley creek where sediments were moist to wet. Observations of liquefaction features within Salt Wells Valley did not appear to impact infrastructure at the base, and no incidents were reported to us during our reconnaissance. Some liquefaction-related features (lateral spreads and three sand boils) were observed in the

Salt Wells Valley area following the **M**6.4 event, but prior to the **M**7.1 mainshock (Figure 2 and S13).

Comparison to Pre-Event Susceptibility Map and Post-Event Liquefaction Hazard Map

Previous studies for liquefaction potential were performed by Banks (1982), by investigating sediments within Indian Wells Valley to evaluate the possibility of seismically induced liquefaction of sediments beneath important structures at the NAWS. Banks' study produced a susceptibility matrix that included age of deposit, soil type, and depth to groundwater. The results from that study concluded that much of the study area has a strong likelihood of liquefaction if earthquake ground motions from a set of 5 sources (Sierra Nevada, Little Lake, Airport Lake, Argus, Garlock, and background seismicity) with a 100-year event return period were to occur. As part of the study, a map was produced showing areas with near-surface sediments having high-, moderate-, and non-susceptible conditions. The Salt Wells Valley was not included in the study by Banks. Portions of the Banks map that overlapped with our study area were digitized and are included in Figure 2. We find that the map successfully identified locations of liquefaction at Paxton Ranch and Southern China Lake, but that it did not predict the liquefaction effects at the margin of China Lake or in the Salt Wells Valley, and predicted large zones of liquefaction susceptibility where no effects were observed during our field visits (i.e., false positives). This overprediction was likely influenced by the map having been derived from older groundwater depths and precipitation catalogues and having limited information on soil type information, factors which control liquefaction susceptibility.

Figure 4 shows the near real-time liquefaction probability map produced by USGS following the **M**7.1 mainshock. The map predicts high probability of liquefaction within China Lake, the Salt Wells Valley, and in the Paxton Ranch area. The spatial distribution of liquefaction surface manifestation in these regions seems to be consistent with the prediction of the liquefaction hazard map. In these areas the predicted probability of liquefaction ranges between 5-20%. In the western portion of Figures 4 and S18, west of China Lake, the predicted probability map does not appear to be consistent with our on-ground and overflight observations.

Trona and Argus

Trona and Argus are situated near the northwestern margin of Searles Lake (Figure 3). Geologic features include lacustrine deposits along the margin of Searles lake, alluvial deposits upslope from the lacustrine deposits, and alluvial fans near the base of the hills to the northwest. Liquefaction features were apparent throughout this region.

Reconnaissance Methods

The GEER Team visited Trona and Argus July 5-7, 2019, and documented evidence of liquefaction using geotagged digital photos and ground-based mapping techniques using tape measures and GPS track logs. A Phase II GEER team subsequently visited sites of interest in Trona and Argus the following week to gather sUAS images that were processed using Structure from Motion techniques to obtain point clouds and digital elevation models. Data from these studies is publicly available and documented by Brandenberg et al. (2020b). The GEER reconnaissance effort did not focus on Searles

Lake due to access restrictions. However, a follow-up visit by a subset of the team in November 2019 with cooperation from Searles Valley Minerals Inc. expanded the locations of observed liquefaction effects (Zimmaro and Hudson, 2019). This reconnaissance effort utilized geotagged photos, GPS track logs, and ground measurements.

Findings

Figure 5 shows locations of observed liquefaction features (sand boils and cracks in hardscape and paving) in Trona and a portion of Searles Lake. Sand boils were encountered along the southern edge of Trona near the northern margin of Searles Lake (e.g., Figure 6a). Sand boils frequently occurred at discontinuities on the ground surface such as pavement edges, utility fixtures, pre-existing cracks (prior to earthquake sequence), and developed cracks (created as a result of the earthquake sequence). Examples of these various sand boil features are available in the accompanying supplements and Brandenberg et al. (2019; 2020b).

Ground cracks caused by extensional strain due to lateral spreading were apparent near the sand boils, and throughout the investigated region (Figure 6: b, c, g). The orientation of the extensional cracks was variable. Many cracks trended toward the northeast, parallel to the lake perimeter, but other cracks were at different angles. We interpret this to indicate that the lateral spreading was predominantly toward the lakebed, but lateral movement occurred in other directions as well, possibly due to the influence of structures on ground displacements, or due to ground oscillation (Figure 6g). In addition to the extensional ground cracks, compressional features were also observed in various regions

(Figure 6: d, e, f, h), as evidenced by buckled concrete curbs, and regions where the asphalt pavement cracked and rode up over adjacent pavement.

Field mapping to record locations of cracks and approximate crack widths were performed along three transects in Trona (shown in Figure 5). Transect TT1 was initiated at Mountain View Street and continued east to Jones Street, ultimately ending near the northeast corner of the Family Dollar store. Transect TT1 is approximately 325 m long with elevations (from Google Earth Pro, see Data and Resources section) that range from 506 - 501 m MSL (west to east), indicating an average ground surface slope along the transect of approximately 1.6%. Figure 7 shows cumulative crack width versus distance along the transect. The sum of the ground crack widths measured along TT1 is 89 cm. Example images of ground cracks along Transect TT1 are shown in Figure 6h. We acknowledge that the sum of crack widths along a transect, as shown in Figure 7, may underestimate lateral movement, due to measurement errors or extensional features that do not manifest as cracks (Rathje et al., 2017a).

As shown in Figure 5, transect TT2 was oriented in a nearly north-to-south direction, starting near the northwest limit of the ground failure region and ending at the Family Dollar parking lot. Transect TT2 is approximately 122 m long with elevations (from Google Earth Pro) that range from 503 - 500 m MSL (north to south-southeast), indicating an average gradient of approximately 2.3%. As shown in Figure 7, the sum of the ground crack widths measured along TT2 is 71 cm. Example images of ground cracks along Transect TT2 are shown in Figure 6c.

Transect TT3 was initiated at the intersection of Magnolia Avenue and Argus Avenue and continued southeast, ending at the intersection of Argus Avenue and Trona Road. Transect TT3 is approximately 53 m long and the elevation difference (from Google Earth Pro) is estimated as 2 m, indicating an average ground surface slope along the transect of approximately 4%. The sum of the ground crack widths measured along TT3 is 45 cm. Example images of ground cracks along Transect TT3 are shown in Figure 6f.

The tension cracks in Trona that are documented in the transects occurred within a region that had been subject to pre-earthquake ground deformations. This was evident from patched cracks in pavement, some of which re-opened during ground shaking. To the extent possible, the field teams sought to document “fresh” cracks that they believed opened during the earthquake, and only those features are included in the transects reported in Figure 7.

Liquefaction-related features were also observed in Argus (Figure 8). The ground surface in the area shown as experiencing liquefaction has a gentle slope. The ground surface exhibited extensional cracks ranging from less than a millimeter to approximately 10 cm in width. The lateral spreading features became less frequent with proximity to the hills west of Argus, and were more pervasive along the axis of a large alluvial fan (Figure 3). A photographic survey was performed along a transect on A Street (designated Transect AT1), approximately along the axis of the alluvial fan (Figure 8). The transect was 457 m long with elevations (from USGS Topographic Map, see Data and Resources section for more details) that range from 499 - 524 m MSL (east to west), indicating an average ground surface slope along the transect of approximately 5%. The extensional features were measured along Transect AT1 in Figure 8, with cumulative crack widths as shown in Figure 7. An example of lateral displacement cracking observed along Transect AT1 is shown in Figure S19. The sum of ground crack widths measured across the 457 m-long transect was approximately 57 cm.

Whereas in Trona the documented lateral spread features were co-located with or nearby sand boils or other liquefaction surface manifestations, ejected material was not observed in Argus. Figure 8b shows Transect AT1 along with the DPM produced following the earthquake sequence. The damage proxy map and ground-based field observations are in good agreement along this transect. At the intersection of A Street (AT1 transect) and Trona Road, non-zero damage proxies occur toward the southwest of the transect. At this location, the DPM helps identify the edges of this lateral spread feature.

A portion of the railroad track that passes through Argus was damaged, apparently by liquefaction-related ground movements, following the earthquake sequence. This feature occurred near the intersection of three different geologic units (gravel and sand, older alluvium, and sand and silt; Brandenberg et al., 2020b). Figure S20a, b shows photos taken on July 6 while repair works were taking place. At this site, tension cracks and lateral spreading openings were visible. An orthomosaic image, point cloud, and digital elevation model of the area (produced following completion of the repair works), showing the railroad repair zone, is available on DesignSafe (Winters et al., 2019).

Ground Failure Effects on Buildings

Structures in the Towns of Trona and Argus appear to have been affected by liquefaction-induced ground failure/movement, primarily from lateral spreading. Figure 9 shows examples of buildings that experienced damage in Trona, some of which may have been liquefaction-related. Figure 9a shows a 2.5 cm-wide crack in the wall connecting the Esparza Restaurant and the adjacent building that occurred as a result of lateral spreading in combination with ground shaking. Figure 9b shows wall cracks on the eastern side of the Esparza Restaurant that has misaligned the door frame and caused the door to remain ajar. Figure 9c and 9d show significant displacement and cracking of a sidewalk due to lateral spreading (there is a 0.5 L plastic bottle within the crack in Figure 9c). Figure 9e and 9f show structural damage in the form of large cracks in the floor slab of a museum due to lateral spreading, while Figure 9d shows a compressional crack in a sidewalk, along with damage to the adjacent building column. Figure 9h shows the Esparza Restaurant, which experienced wall cracks from lateral spreading in the **M**6.4 event that were widened in the **M**7.1 event, which the GEER team photographed after each event. It is possible that some of the observed cracks pre-dated the earthquake sequence and were subsequently widened by the earthquake. The crack shown in Figure 9h on the eastern wall of the Esparza Restaurant building continued up to the roof, and the roof diaphragm was pulled apart, as shown in Figure 9i. Apparent effects of liquefaction on structures also occurred in Argus where structures that were heavily damaged were located on or near the alluvial fan, which exhibited evidence of lateral spreading in the form of tension cracks. Structural damage took the form of chimney separations from buildings, masonry cracks from extensional movements, toppled walls, and punch-through in retention walls (Stewart et al. 2019).

Searles Lake

Searles Lake is a source of mineral-rich resources, which are mined by Searles Valley Minerals Inc. Main extraction activities at Searles Lake are based on solution mining operations involving wells that are used to pump out brine. The brine is then processed to produce products such as salt, borax, boric acid, and sodium sulfate. Since a portion of the lake (mainly in the northwest area, next to Trona) is used continuously for mining activities, authorization is required to access the area. The first GEER team deployed in the region in July 2019 did not enter the mining zone.

Reconnaissance Methods

As shown in Figure 1, the DPM produced following the Ridgecrest earthquake sequence indicates significant surface change within the Searles Lake area. High concentrations of non-zero SAR-based damage proxies are typically indicative of substantial damage/ground deformation. As a result, a second team (1st and 4th authors) requested and obtained authorization to access the area on November 19 2019 to perform reconnaissance to evaluate potential ground deformations in the area. The areas of the lake visited during this reconnaissance mission are outside of the mining activity zones and no extreme weather events occurred in the time between the earthquake mainshock and field deployment. As a result, we do not anticipate that the delay impacted our ability to document liquefaction features. Reconnaissance activities were performed with the assistance of Searles Valley Minerals personnel. This reconnaissance effort was performed utilizing geotagged photos, GPS track logs, and ground measurements.

Results of this reconnaissance mission (maps and photographs) are available on DesignSafe (Zimmaro and Hudson, 2019).

Since the lake area is large (roughly 16 by 9 km), priority zones were selected using the DPM (Figure S21). Non-zero damage proxies may be related to any surface changes. Since mining activities are concentrated in the northwest area of the lake, this zone may present surface changes from both earthquake-related ground failures and human activities. Our observations were made outside of the zones of mining activity, and hence are anticipated to result from earthquake-related ground failure.

The DPM in Figure 10 shows non-zero damage proxies roughly aligned with the lake margins. Portions of the lake boundary that exhibit such patterns include the north-west edge of the lake and two semi-circular concentric zones in the south-west area of the lake. In the area of the lake south-west of Trona a large portion of the lake is covered by a cluster of non-zero damage proxies, while in the area south-west of Argus, a large number of proxies are aligned along the lake margin. Figure 11 shows the USGS near real-time liquefaction hazard map produced following the **M**7.1 mainshock. This map shows high probability of liquefaction in the central zone of the lakebed. It predicts low or no liquefaction hazard along the lake margins.

Findings

Figure 10 shows the track log from the reconnaissance and locations of geotagged photos. Figure 10 also provides an overview of the reconnaissance findings. Figure 12a shows a photo of the central zone of the eastern edge of the lake (Zone 1 in Figure 10). This photo was taken from the road located southwest of the linear damage zone highlighted by the DPM. It shows a relatively narrow (about 110 m wide) zone covered by greyish ejecta with different coloration than surrounding material. This zone is potentially useful to study liquefaction susceptibility as it is a clear example of variable liquefaction performance over a short length scale. At this location the probability of liquefaction predicted by the USGS liquefaction hazard map is ~4%.

Massive liquefaction was observed near the southwest edge of the lake (labelled Zone 2 in Figure 10). Thousands of sand boils (Figure 12c), ground fissures and cracks (Figure 12d), and abundant sand, gravel (Figure 12d,e), and brine-evaporite ejecta (Figure 12f) were observed along the relatively narrow NW-SE line depicted on the DPM. We use the term brine-evaporite to indicate that after the brine fluid was ejected onto the surface, evaporites precipitated out of the solution as it evaporated. Figure 12f shows a sand boil entirely covered by a thin brine-evaporite layer. This sand boil covers an area containing sand from two smaller (and older) boils. Two hypotheses can be formulated to explain this phenomenon: (1) both manifestations occurred during the same event - the smaller sand boils were caused by liquefaction occurring in a more surficial layer, while the brine boil occurred in a deeper layer, or (2) the two liquefaction manifestations were triggered by separate events. The correct hypothesis cannot be identified from the available data, because reconnaissance was performed following the major events in the earthquake sequence. Within Zone 2, the USGS liquefaction hazard map predicts a probability of liquefaction ranging between 5-8%.

Widespread liquefaction manifested in hundreds of sand boils, cracks, and fissures was observed in the area southeast of Trona (highlighted in Figure 10). Ground movements are also indicated in this area by the DPM. Similar observations were made on the northwest edge of the lake. In this broad north-northwestern zone of the lakebed, the USGS liquefaction hazard map predicts low (1-2%) or zero probability of liquefaction.

Observations at Searles Lake confirmed ground deformation patterns reported in the DPM. The USGS liquefaction hazard map predicts liquefaction in the lakebed region but the actual observed deformation patterns are not consistent with the map. The mismatch is especially pronounced along the margin of the lakebed where liquefaction was observed at various locations, but predicted liquefaction probabilities are low. Zones 1 and 2 in Figure 10 represents clear examples of DPM true positives (areas where non-zero damage proxies are present and ground failure features are observed). True positives from the DPM were also observed in the area immediately southwest of Trona and at the southwest edge of the lakebed. Some spot checks were performed to identify potential true negatives (areas where colored damage proxies are not present and no ground deformations are observed). Such occurrences were observed in at least four zones in the south and southwest zones of the lakebed (labelled as “No damage” in Figure 10). Neither DPM false positives (areas where non-zero damage proxies are present but no ground deformations are observed), nor DPM false negatives (areas where non-zero damage proxies are not present but ground deformations are observed) were observed at Searles Lake. However, these outcomes do not represent a comprehensive validation of the DPM at Searles Lake as many areas were not accessed and inspected. Nonetheless, these preliminary findings are encouraging regarding the effectiveness of DPMs for the no-vegetation conditions in the Searles Lake area. False positives were also observed in the USGS liquefaction hazard maps. At two of the four locations labelled as “No damage” in Figure 11 (west of Zone 1), the USGS liquefaction hazard map predicted a relatively high probability of liquefaction of ~10%. This map correctly predicted a low (1-3%) probability of liquefaction at a location east of Zone 1, where no damage was observed.

In earlier sections of this paper, we have presented many location-specific field observations and noted the degree of agreement with DPMs or USGS Liquefaction Hazard maps. Here we seek to assemble the available findings. Doing so requires that the potential liquefaction effects can be separated from other effects in the DPMs – arguably this is not the case for the China Lake sites (due to proximity to surface rupture, which produces large movements that obscure liquefaction features) and human-occupied regions such as Trona and Argus (where anthropogenic effects add noise to the maps). This leaves the Searles Lake sites as providing the optimal conditions for the comparison.

We focus on the southern portion of the lakebed, south of 35.74°, where we have six sites where liquefaction was observed and five sites without ground failure. For the purpose of the quantitative comparison, we use a 0.5% probability of liquefaction threshold for the USGS maps (i.e., ≥ 0.5% = liquefaction, < 0.5% = no ground failure) and pixels with colorations for the DPMs. Based on these thresholds, the "correct" predictions of field observations are made 10 of 11 times (~90%) for DPM and 5 of 11 times for the USGS map (~50%). Using a higher threshold probability of liquefaction, equal to 5%, results are similar (correct predictions are made 5 of 11 times).

There are alternative means by which the utility of USGS maps can be assessed. Arguably, their purpose is not to identify specific locations of liquefaction/no-ground failure, but rather to highlight broader regions where liquefaction may or may not have occurred. Viewed from this perspective, region-wide quantitative metrics may be useful to assess performance. Again returning to the southern region of Searles Lake (surface area of 94.8 km^2), the percentage of land area identified by the DPM to have deformations is 18.7% (17.7 km^2), which given the favorable performance of DPMs to field observations, can be taken as rough estimate of the percentage of land affected by liquefaction. The percentage of land area with probability of liquefaction greater than 5% and 10% from the USGS liquefaction hazard map is 57.3% (54.4 km^2) and 18.0% (17.1 km^2), respectively. These figures broadly agree with the field performance. Hence, while the USGS maps do not predict at a high percentage the specific locations of liquefaction, they do appear to correctly asses the percentage of affected land within the broader lakebed geomorphic province.

Summary and Research Significance

We present liquefaction and related ground failures triggered by the 2019 Ridgecrest earthquake sequence. Observations presented in this paper were collected as a result of a multi-agency interdisciplinary collaboration between GEER, CGS, USGS, and NASA. We present data on liquefaction manifestations including lateral spread features, sand boils, pavement cracks, fissures, and sand and gravel ejecta in three regions: (1) within Naval Air Weapons Station China Lake, (2) in the towns of Trona and Argus located on the northeast margin of Searles Lake, and (3) within the interior of Searles Lake. Data collected in Trona, Argus, and the naval base were collected in July-August 2019 during the GEER deployment, while data within Searles Lake were collected in November 2019.

The latter deployment was organized using SAR-based DPMs as a guidance tool for planning and identification of priority areas.

The documentation of field performance presented in this paper comprises one component of a liquefaction case history, with remaining components (not developed here) being ground motion demands and geotechnical site conditions. With future work to develop those attributes, we anticipate that the data presented here can impact future liquefaction models in the following respects:

- The well-documented lateral spread features in Trona and Argus along four transects can contribute to the development of lateral spread models for “ground slope” (not free-face) conditions.
- Variable ground performance with respect to the manifestation of liquefaction-induced ground failure over short length scales at the edge of Searles Lake could provide valuable insights into how subtle changes in soil composition or depositional environment affect liquefaction susceptibility.
- Ground failure-related building damage in Trona and Argus. Such data may inform future models for effects of soil-structure-interaction on building performance with liquefiable foundation soils.

Furthermore, the data presented in this paper constitutes a valuable resource for validating SAR-based DPMs and near real-time liquefaction hazard maps. The USGS liquefaction probability maps are generated in near real-time following major earthquakes, while DPMs are produced within a matter of days following extreme events (including hurricanes, earthquakes, and wildfires). Both maps are still being calibrated and validated against observed damage. Thus, ground truth information is key for improving these products and their reliability in detecting post-event damage. Quantitative assessment of the performance of these maps shows that DPMs identify specific locations and areas where surface change occurred. However, these maps cannot discern among different sources of deformations. The DPM performed particularly well in the southern portion of Searles Lake where earthquake-induced surface changes were mostly related to liquefaction surface manifestations. More work is needed to quantitatively correlate raw coherence loss values with the percentage land covered by liquefaction surface manifestations (i.e., by using high-resolution satellite imagery). The USGS liquefaction hazard map, does not identify specific liquefaction or no-ground failure locations accurately, but it is effective at identifying broad percentages of land with ground failure in an impacted geomorphic province (Searles lake bed).

Data and Resources

Moment tensors for the **M**6.4 and **M**7.1 events were retrieved from the USGS event pages at: https://earthquake.usgs.gov/earthquakes/eventpage/ci38443183/moment-tensor and https://earthquake.usgs.gov/earthquakes/eventpage/ci38457511/moment-tensor, respectively (last accessed on January 14, 2020). Fault traces from the Uniform California Earthquake Rupture Forecast, Version 3 (UCERF3) model were retrieved from the CGS open data portal at: https://data.ca.gov/dataset/cgs-map-sheet-48-fault-based-seismic-sources-used-in-the-uniform-california-earthquake-rupture (last accessed on May 1, 2020). The Damage proxy map used was retrieved from the NASA ARIA-JPL event page at: https://aria-share.jpl.nasa.gov/20190704-0705-Searles_Valley_CA_EQs/DPM/ (last accessed on January 14, 2020). The USGS liquefaction probability map produced following the M7.1 mainshock was retrieved from the USGS event page at: https://earthquake.usgs.gov/earthquakes/eventpage/ci38457511/ground-failure/summary (last accessed on May 1, 2020). Observation wells data were retrieved from the California DWR database at: http://wdl.water.ca.gov/waterdatalibrary/groundwater/hydrographs/brr_hydro.cfm?CFGRIDKEY=23361 (last accessed on May 1, 2020). The USGS topographic map was retrieved from the USGS National Geospatial Program – US Topo at: https://www.usgs.gov/core-science-systems/national-geospatial-program/us-topo-maps-america?qt-science_support_page_related_con=0# (last accessed on May 1, 2020). Elevation data were retrieved from Google earth pro (https://www.google.com/earth/versions/#earth-pro, last accessed on May 7, 2020). All maps were produced using QGIS (QGIS Development Team, 2020, QGIS Geographic Information System. Open Source Geospatial Foundation Project, http://qgis.osgeo.org, last accessed on January 14, 2020). A summary table of observations at the Naval Air Weapons Station, China Lake and 18 Figures showing liquefaction features at the at the Naval Air Weapons Station, China Lake and Argus are available in the electronic supplement to this paper.

Acknowledgements

The GEER Association is supported by the National Science Foundation (NSF) through the Geotechnical Engineering Program under Grant No. CMMI-1266418. Any opinions, findings, and conclusions or recommendations expressed in this material are those of the authors and do not necessarily reflect the views of the NSF. The GEER Association is made possible by the vision and support of the NSF Geotechnical Engineering Program Directors: Richard Fragaszy and the late Cliff Astill. GEER members also donate their time, talent, and resources to collect time-sensitive field observations of the effects of extreme events. Part of the research was sponsored by the NASA Earth Science Disasters Program (Grant No: 18-DISASTER18-0034) and performed in collaboration with the Jet Propulsion Laboratory, California Institute of Technology. The authors would like to thank Camille Anderson, Steven Kourakos, Adam Bingham, Dipti Barari, Devin Katzenstein at Searles Valley Minerals and Jade Zimmerman at China Lake Naval Air Weapons Station for assisting with the preparation and deployment of reconnaissance activities at Searles Lake in November 2019.

References

Allstadt, K. E., E. M. Thompson, M. Hearne, J. Zhu, D. J. Wald, and H. Tanyaş (2017). Integrating landslide and liquefaction hazard and loss estimates with existing USGS real-time earthquake information products, Proc. 16th World Conf. Earthquake Eng., Santiago, Chile, 9–13 January 2017, Paper 364.

Baise, L. G., and V., Rashidian (2017). Validation of a Geospatial Liquefaction Model for Noncoastal Regions Including Nepal: Final Technical Report for USGS Award G16AP00014.

Banks, E. W. (1982). Soil Liquefaction Potential at the Naval Weapons Center China Lake, California, University of Nevada Reno Master's Thesis, NWC Technical Publication 6392, September, 1982, 106 p., 4 plates.

Barnhart, W. D., G.P. Hayes, and R.D. Gold (2019). The July 2019 Ridgecrest, California, earthquake sequence: Kinematics of slip and stressing in cross-fault ruptures. *Geophy. Res. Letters* **46**, 11859–11867.

Berenbrock C., and R. A. Schroeder (1991). The Ground-Water Flow and Quality, and Geochemical Processes, *in* Indian Wells Valley, Kern, Inyo, and San Bernardino Counties, California, 1987-88. U.S. Geological Survey Open-File Report, 36 p.

Brandenberg S. J., P. Zimmaro, J. P. Stewart, D. Y. Kwak, K. W. Franke, R. E. S. Moss, K. O. Cetin, G. Can, M. Ilgac, J. Stamatakos, T. Weaver, S. L. Kramer (2020a). Next Generation Liquefaction Database, *Earthquake Spectra*. DOI: 10.1177/8755293019902477.

Brandenberg, S. J., C. A. Goulet, P. Wang, C. C. Nweke, C. A. Davis, M. B. Hudson, K. S. Hudson, S. K. Ahdi, J. P. Stewart (2019) GEER Field Reconnaissance, in *Ridgecrest, CA earthquake sequence, July 4 and 5, 2019*. DesignSafe-CI. https://doi.org/10.17603/ds2-vpmv-5b34.

Brandenberg, S. J., J. P. Stewart, P. Wang, C. C. Nweke, K. S. Hudson, C. A. Goulet, X. Meng, C. A. Davis, S. K. Ahdi, M. B. Hudson, et al. (2020b). Ground Deformation Data from GEER Investigations of Ridgecrest Earthquake Sequence, *Seismol. Res. Lett.*, DOI: 10.1785/0220190291.

Bullard, T., S. Bacon, K. Adams, and D. Decker (2019). Geomorphic Map of the China Lake Basin Below 700 m in Support of Cultural Resource Management at Naval Air

Weapons Station China Lake. NAWCWD TM 8839. Desert Research Institute Reno United States. https://apps.dtic.mil/dtic/tr/fulltext/u2/1077596.pdf

California Department of Water Resources (2003). *California's Groundwater*, Bulletin 118, Update 2003.

California Department of Water Resources (2020). Water Data Library, accessed January 2, 2020, http://wdl.water.ca.gov/waterdatalibrary/.

Dawson, T., C. B. DuRoss, R. Gold, K. Scharer, D. Ponti, T. Ladinsky, V. E. Langenheim, D. McPhillips, A. Morelan, C. Milliner, et al. (2020). Field-based Observations of Surface Ruptures Associated with the 2019 Ridgecrest Earthquake Sequence; in preparation for *Bull Seismol Soc Am*.

Fan, Y., H. Li, and G. Miguez-Macho (2013). Global Patterns of Groundwater Table Depth: *Science* **339**, 940-943.

Field, E. H., R. J. Arrowsmith, G. P. Biasi, P. Bird, T. E. Dawson, K. R. Felzer, D. D. Jackson, K. M. Johnson, T. H. Jordan, C. Madden, et al. (2014). Uniform California earthquake rupture forecast, version 3 (UCERF3)—the time-independent model, *Bull Seismol Soc Am* **10**, 1122–1180.

Fielding, E. J., M. Talebian, P. A. Rosen, H. Nazari, A. Jackson, M. Ghorashi, and R. Walker (2005). Surface ruptures and building damage of the 2003 Bam, Iran, earthquake mapped by satellite synthetic aperture radar interferometric correlation, *J. Geophys. Res.* **110**, B03302.

Franke, K.W., B. N. Lingwall, P. Zimmaro, R. E. Kayen, P. Tommasi, F. Chiabrando, and A. Santo (2018). A phased reconnaissance approach to documenting landslides following the 2016 Central Italy earthquakes, *Earthquake Spectra* **34**, 1693–1719.

Hijmans, R. J., S. E. Cameron, J. L. Parra, P. G. Jones, and A. Jarvis (2005). Very high resolution interpolated climate surfaces for global land areas, *International Journal of Climatology* **25** no. 15, 1965–1978.

Ishitsuka, K., T. Tsuji, and T. Matsuoka. (2012). Detection and mapping of soil liquefaction in the 2011 Tohoku earthquake using SAR interferometry, *Earth, Planets and Space* **64**, Article number: 22.

Jennings, O.P., J. L. Burnett, and B. W. Troxel (1962). Geologic Map of California-Trona Sheet, California Division of Mines and Geology (California Geological Survey), GAM 023, Map Scale 1:250,000.

Jibson, R. W. (2020). Types and areal distribution of ground failure associated with the 2019 Ridgecrest, California, earthquake sequence. *Bull Seismol Soc Am*. doi: 10.1785/0120200001.

Jung, J., and S. –H. Yun (2020). Evaluation of coherent and incoherent landslide detection methods based on synthetic aperture radar for rapid response: a case study for the 2018 Hokkaido landslides. *Remote Sens* **12** no. 2, 265.

Kunkel, F., and G. H. Chase (1969). Geology and ground water in Indian Wells Valley, California, U.S. Geological Survey Open-File Report, 84 p.

Lancaster, N., N. S. Bacon, T. F. Bullard, S. E. Baker, D. L. and Decker (2019). Eolian Hazard Assessment for the SNORT Facility (U). No. NAWCWD TP 8840. Desert Research Institute Reno United States. https://apps.dtic.mil/dtic/tr/fulltext/u2/1077597.pdf

McGraw, D., R. Carroll, G. Pohll, J. Chapman, S. Bacon, and R. Jasoni (2016). Groundwater Resource Sustainability: Modeling Evaluation for the Naval Air Weapons Station, China Lake, California: Prepared by Desert Research Institute for Naval Air Warfare Center Weapons Division.

Ponti, D.J., J. L. Blair, C. M. Rosa, K. Thomas, A. J. Pickering, S. Akciz, S. Angster, J. – P. Avouac, J. Bachhuber, S. Bacon, et al. (2020). Documentation of surface fault rupture and ground deformation features produced by the Ridgecrest M6.4 and M7.1 earthquake sequence of July 4 and 5, 2019, *Seismological Research Letters*, in press.

Rathje, E. M., C. Dawson, J. E. Padgett, J. –P. Pinelli, D. Stanzione, A. Adair, P. Arduino, S. J. Brandenberg, T. Cockerill, M. Esteva, et al. (2017a). DesignSafe: A new cyberinfrastructure for natural hazards engineering, *Natural Hazards Review* **18** no. 3, 06017001.

Rathje, E. M., S. S. Secara, J. G. Martin, S. van Ballegooy, and J. Russell (2017b). Liquefaction induced horizontal displacements from the Canterbury earthquake sequence in New Zealand measured from remote sensing techniques, *Earthquake Spectra* **33**, 1475-1494.

Schweig, E. S., III (1984). Neogene tectonics and paleogeography of the southwestern Great Basin, Inyo County, California: Palo Alto, California, Stanford University, Ph.D. dissertation, 207p.

Sextos, A., R. De Risi, A. Pagliaroli, S. Foti, F. Passeri, E. Ausilio, R. Cairo, M. C. Capatti, F. Chiabrando, A. Chiaradonna, et al. (2018). Local patterns and incremental damage of buildings during the 2016 Central Italy earthquake sequence, *Earthquake Spectra* **34**, 1639–1669.

Smith, G. I. (1979). Subsurface stratigraphy and geochemistry of late Quaternary evaporites, Searles Lake, California: U.S. Geological Survey Professional Paper 1043, 130 p.

Smith, G. I. (2009). Late Cenozoic Geology and Lacustrine History of Searles Valley, Inyo and San Bernardino Counties, California: U.S. Geological Survey Professional Paper 1727, 115 p., 4 plates.

Schmitt, R. G., H. Tanyas, M. A. Nowicki Jessee, J. Zhu, K. M. Biegel, K. E. Allstadt, R. W. Jibson, E. M., Thompson, C. J. van Westen, H. P. Sato, et al. (2017). An Open Repository of Earthquake-Triggered Ground-Failure Inventories (ver 2.0, December 2018), U.S. Geological Survey data release collection. DOI: 10.5066/F7H70DB4.

Stewart, J. P. (Editor), S. J. Brandenberg, P. Wang, C. C. Nweke, K. S. Hudson, S. Mazzoni, Y. Bozorgnia, K. W. Hudnut, C. A. Davis, S. K. Ahdi, et al. (2019). Preliminary report on engineering and geological effects of the July 2019 Ridgecrest Earthquake sequence, Geotechnical Extreme Events Reconnaissance Association, *Rept. GEER-064*, DOI: 10.18118/G6H66K.

U. S. Geological Survey (USGS) (2020). Earthquake Catalog. Available at: https://earthquake.usgs.gov/earthquakes/search/. Last accessed 04/30/2020.

Wald, D. J., C. B. Worden, V. Quitoriano, and K. L. Pankow (2005). ShakeMap manual: Technical manual, user's guide, and software guide. U.S. Geological Survey, Techniques and Methods 12-A1. Available at: http://pubs.usgs.gov/tm/2005/12A01/ (last accessed May 1, 2020).

Wald, D. J., and T. I. Allen (2007). Topographic Slope as a Proxy for Seismic Site Conditions and Amplification. *Bull Seismol Soc Am* **97** no. 5, 1379–1395.

Warner, J. W. (1975). Ground-water quality in Indian Wells Valley, California: U.S. Geological Survey Water Resources Investigations Report 8-75, 59 p.

Winters, M. A., M.-P. C. Delisle, J. T. D. Lucey, Y. Kim, Z. Liu, K. S. Hudson, S. J. Brandenberg, and T. W. Gallien (2019). UCLA UAV imaging, Ridgecrest, CA Earthquake Sequence, July 4 and 5, 2019, Designsafe-CI, DOI: 10.17603/ds2-wfgc-a575.

Worden, C. B., and D. J. Wald (2016). ShakeMap manual online: Technical manual, user's guide, and software guide. U.S. Geological Survey. DOI: 10.1234/012345678. Available at: http://usgs. github.io/shakemap (last accessed May 1, 2020).

Yun, S., E. J. Fielding, M. Simons, P. Rosen, S. Owen, and F. Webb (2011). Damage proxy map of February 2011 M6.3 Christchurch earthquake using InSAR coherence, *8th*

International Workshop on Advances in the Science and Applications of SAR Interferometry, Frascati, Italy, available at https://earth.esa.int/documents/10174/1567329/Yun_FRINGE2011.pdf (last accessed 14 January 2020).

Yun, S., K. Hudnut, S. Owen, F. Webb, M. Simons, P. Sacco, E. Gurrola, G. Manipon, C. Liang, E.J. Fielding, P. Milillo, H. Hua, and A. Coletta (2015). Rapid damage mapping for the 2015 Mw 7.8 Gorkha earthquake using synthetic aperture radar data from COSMO–SkyMed and ALOS-2 Satellites, *Seismol. Res. Letters* **86**, 1549–1556.

Zhu, J., L. G. Baise, and E. M. Thompson (2017). An Updated Geospatial Liquefaction Model for Global Application, *Bull Seismol Soc Am* **107**, 1365-1385. doi: 0.1785/0120160198.

Zhu, J., D. Daley, L. G. Baise, E. M. Thompson, D. J. Wald, and K. L. Knudsen (2015). A geospatial liquefaction model for rapid response and loss estimation: *Earthquake Spectra* **31**, no. 3, 1813–1837.

Zimmaro, P. and Hudson, K. (2019). Searles Lake Liquefaction, in Ridgecrest, CA earthquake sequence, July 4 and 5, 2019. DesignSafe-CI, Dataset. DOI: 10.17603/ds2-9wp5-rp81.

List of Figure Captions

Figure 1. Overview of the Ridgecrest 2019 earthquake sequence epicentral area showing mapped surface fault rupture features following the **M**6.4 and **M**7.1 events (from Ponti et

al., 2020) and locations of surface change as provided on a Damage proxy map produced following the **M**7.1 event. Fault traces are from the Uniform California Earthquake Rupture Forecast, Version 3 (UCERF3) model (Field et al., 2014). Observation well data were obtained from California Department of Water Resources (DWR). Moment tensors were obtained from USGS (see Data and Resources Section). Outlines of detailed maps in Figures 2-3 shown.

Figure 2. Surface geologic map of eastern portion of Indian Wells Valley showing locations of mapped liquefaction features. Liquefaction susceptibility zones modified from mapping by Banks (1982).

Figure 3. Map of the northwestern portion of Searles Valley showing the general geologic material underlying the towns of Trona and Argus. The estimated extent of the dry Searles Lake is also depicted.

Figure 4. Map of the Indian Wells Valley, observed liquefaction features, and USGS near real-time liquefaction hazard map.

Figure 5. Map of Trona showing locations of observed liquefaction effects and lateral spreading measurement transects overlayed on (a) surface geology map and (b) damage proxy map. Geologic units are labeled following descriptions from Smith (2009).

Figure 6. Ground failure from liquefaction in Trona. (a) Sand boil along a pavement crack created from lateral spreading (35.757483°, -117.37806°). (b, c) Extensional cracks caused by lateral spreading (35.757325°, -117.377705°; 35.75966°, -117.375892°). (d, f) Damaged asphalt from buckled curb edge (35.75936°, -117.37676°; 35.762387°, -

117.372586°). (e, h) Compressional features from lateral spreading (35.75897°, -117.37561°; 35.75909°, -117.37552°). (g) compressional and adjacent extensional features/cracks caused by lateral spreading and ground oscillation (35.75986°, -117.37651°).

Figure 7. Cumulative crack width along transects in Trona and Argus. Transection locations are shown in Figures 4 and 7.

Figure 8. Map of Argus showing locations of observed liquefaction effects and lateral spreading measurement transects overlayed on (a) surface geology map and (b) damage proxy map. Geologic units are labeled following descriptions from Smith (2009).

Figure 9. Ground failure effects on buildings in Trona. (a) Crack at screen wall between two buildings (35.75979°, -117.376315°). (b, h, i) Wall cracks at the eastern side of the Esparza restaurant with associated sand ejecta and roof damage (35.75957°, -117.37611°). (c, g) Sidewalk pavement crack and offset likely from lateral spreading and ground oscillation (35.75982°, -117.37637°; 35.75980°, -117.37606°). (e, f) Cracks in floor slab from lateral spreading and ground oscillation (35.759802°, -117.376808°).

Figure 10. Damage proxy map produced following the **M**7.1 event, route of the November 2019 reconnaissance mission, geotagged photo locations, and reconnaissance findings.

Figure 11. USGS liquefaction hazard map produced following the **M**7.1 event, route of the November 2019 reconnaissance mission, geotagged photo locations, and reconnaissance findings.

Figure 12. (a) Narrow liquefaction ejecta zone located in the central portion of the northeast edge of Searles Lake (35.72701°, -117.27801°), (b-f) fissures, sand boils with

sand, gravel, and brine-evaporite ejecta observed towards the southwestern edge of the lake (35.694858°, -117.339622°; 35.6955°, -117.34235°; 35.695913°, -117.34113°; 35.695208°, -117.340462°; 35.695217°, -117.341072°).

Figures

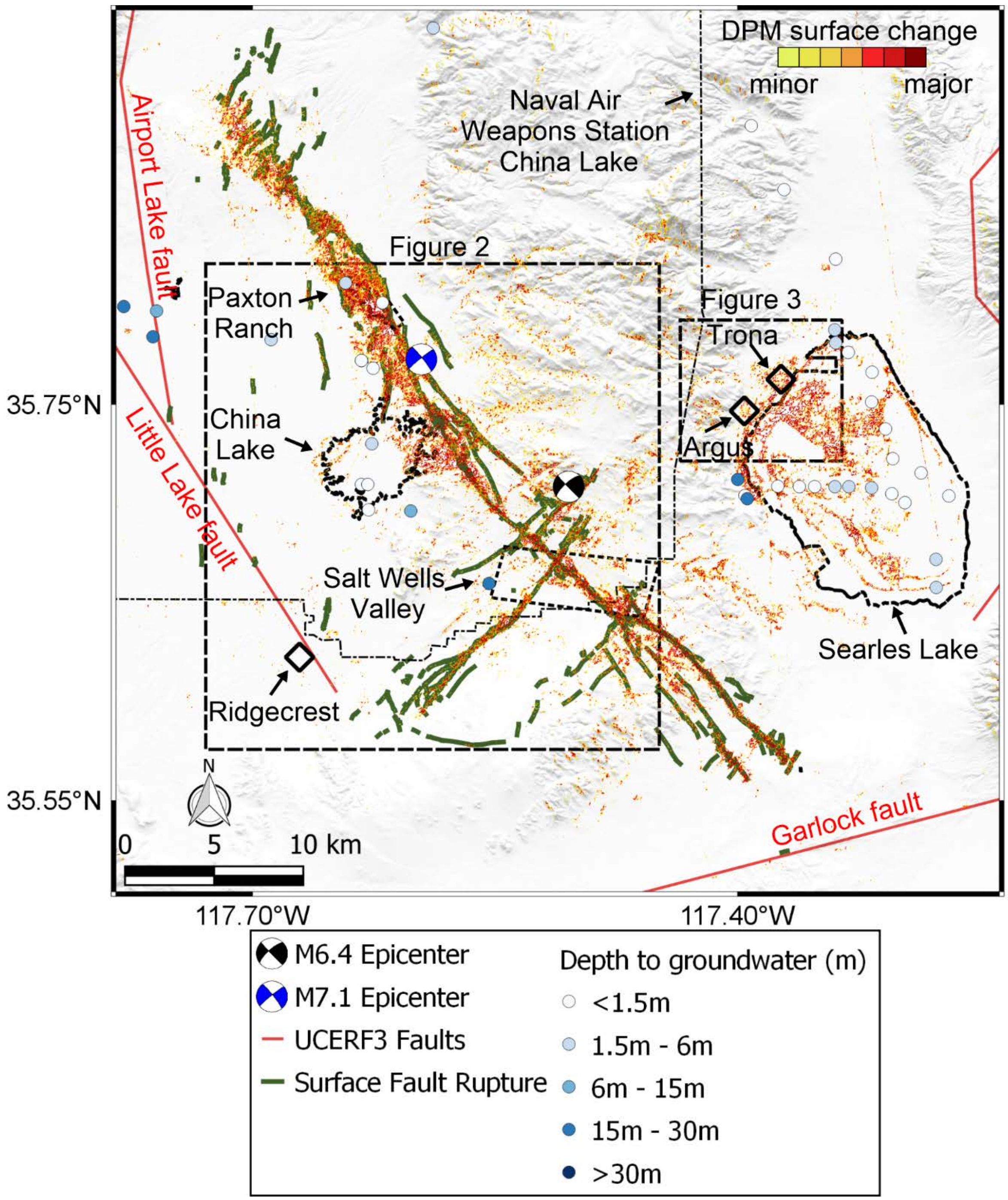

Figure 1. Overview of the Ridgecrest 2019 earthquake sequence epicentral area showing mapped surface fault rupture features following the **M**6.4 and **M**7.1 events (from Ponti et

al., 2020) and locations of surface change as provided on a Damage proxy map produced following the **M**7.1 event. Fault traces are from the Uniform California Earthquake Rupture Forecast, Version 3 (UCERF3) model (Field et al., 2014). Observation well data were obtained from California Department of Water Resources (DWR). Moment tensors were obtained from USGS (see Data and Resources Section). Outlines of detailed maps in Figures 2-3 shown.

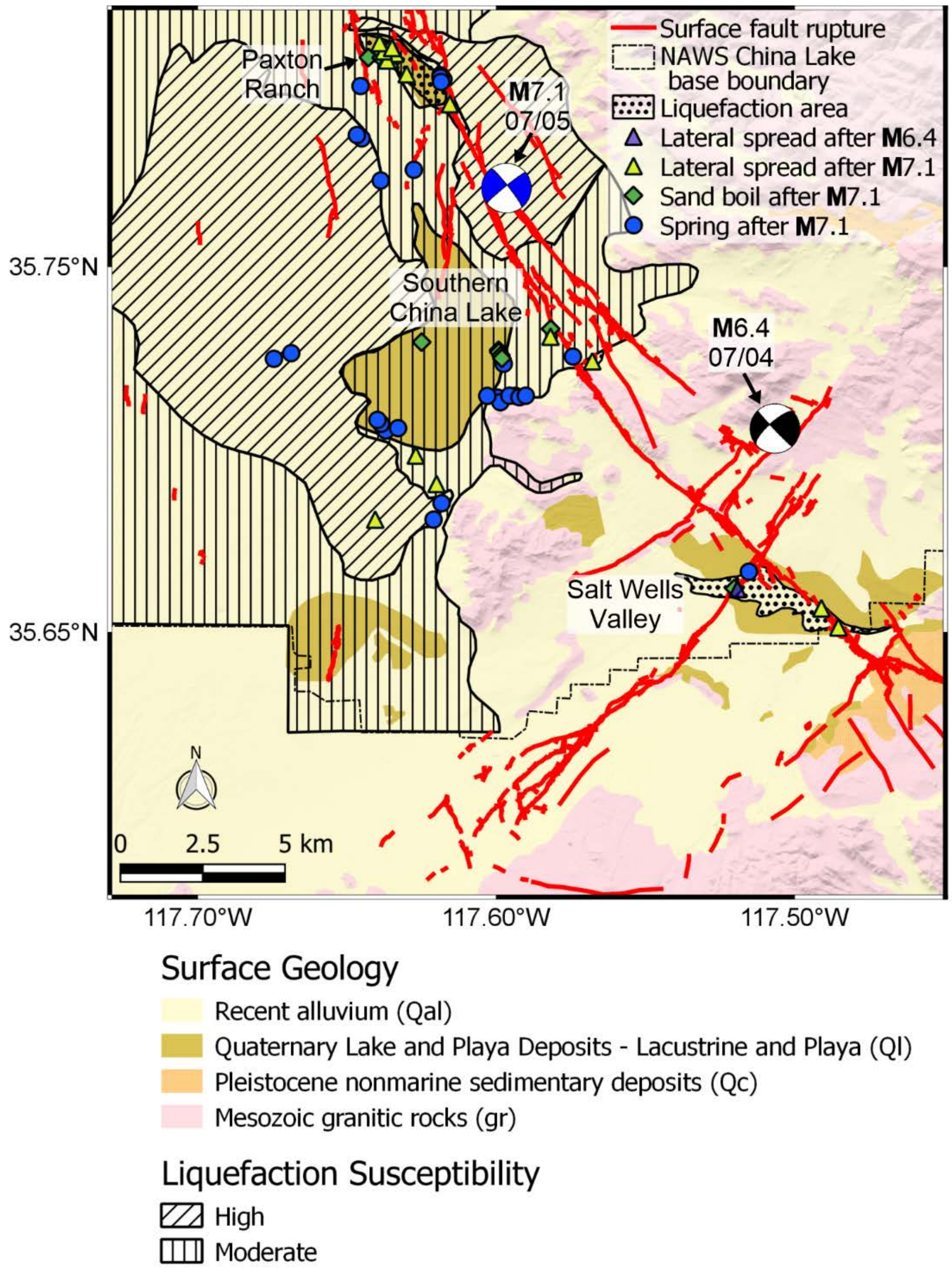

Figure 2. Surface geologic map of eastern portion of Indian Wells Valley showing locations of mapped liquefaction features. Liquefaction susceptibility zones modified from mapping by Banks (1982).

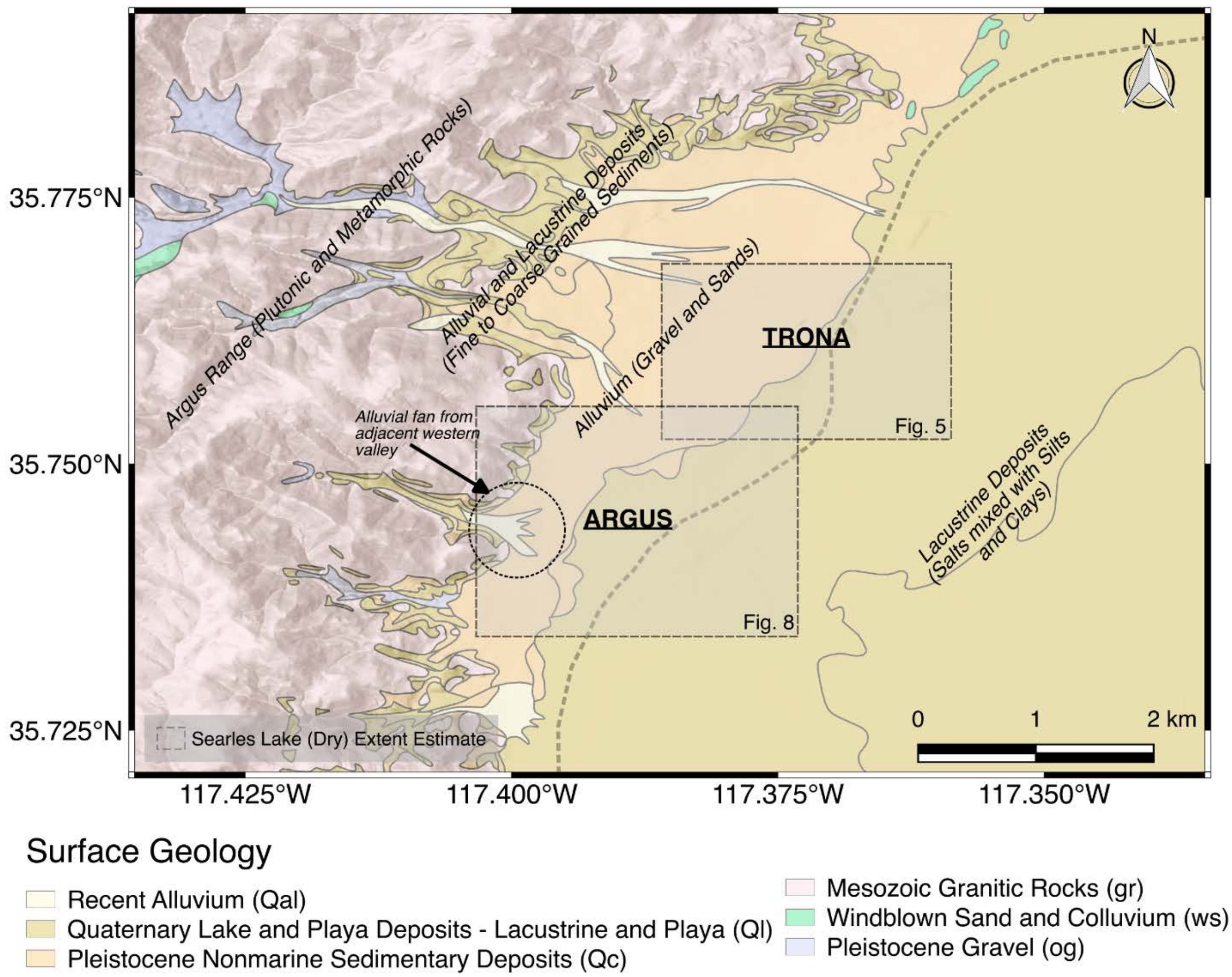

Figure 3. Map of the northwestern portion of Searles Valley showing the general geologic material underlying the towns of Trona and Argus. The estimated extent of the dry Searles Lake is also depicted.

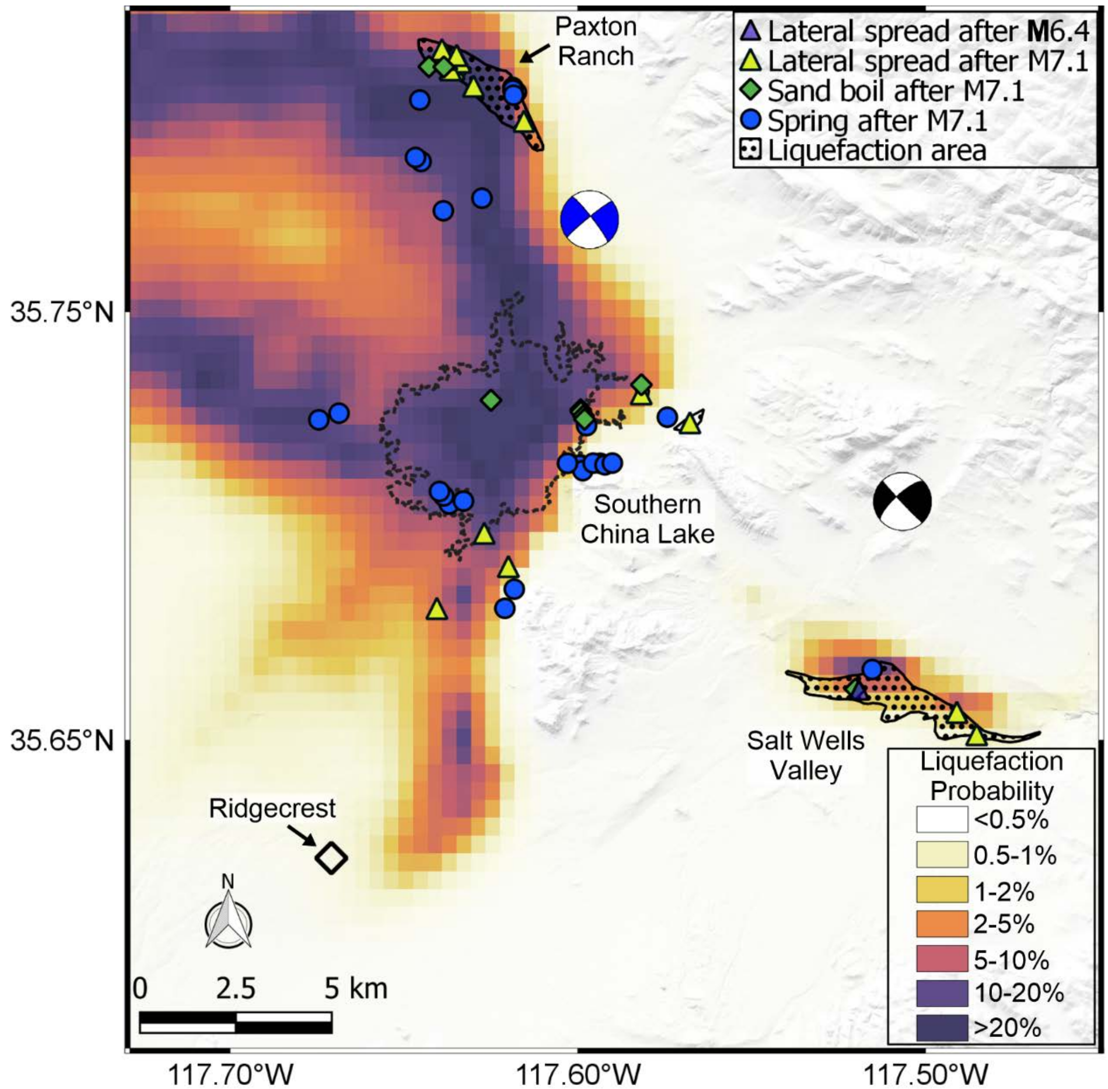

Figure 4. Map of the Indian Wells Valley, observed liquefaction features, and USGS near real-time liquefaction hazard map.

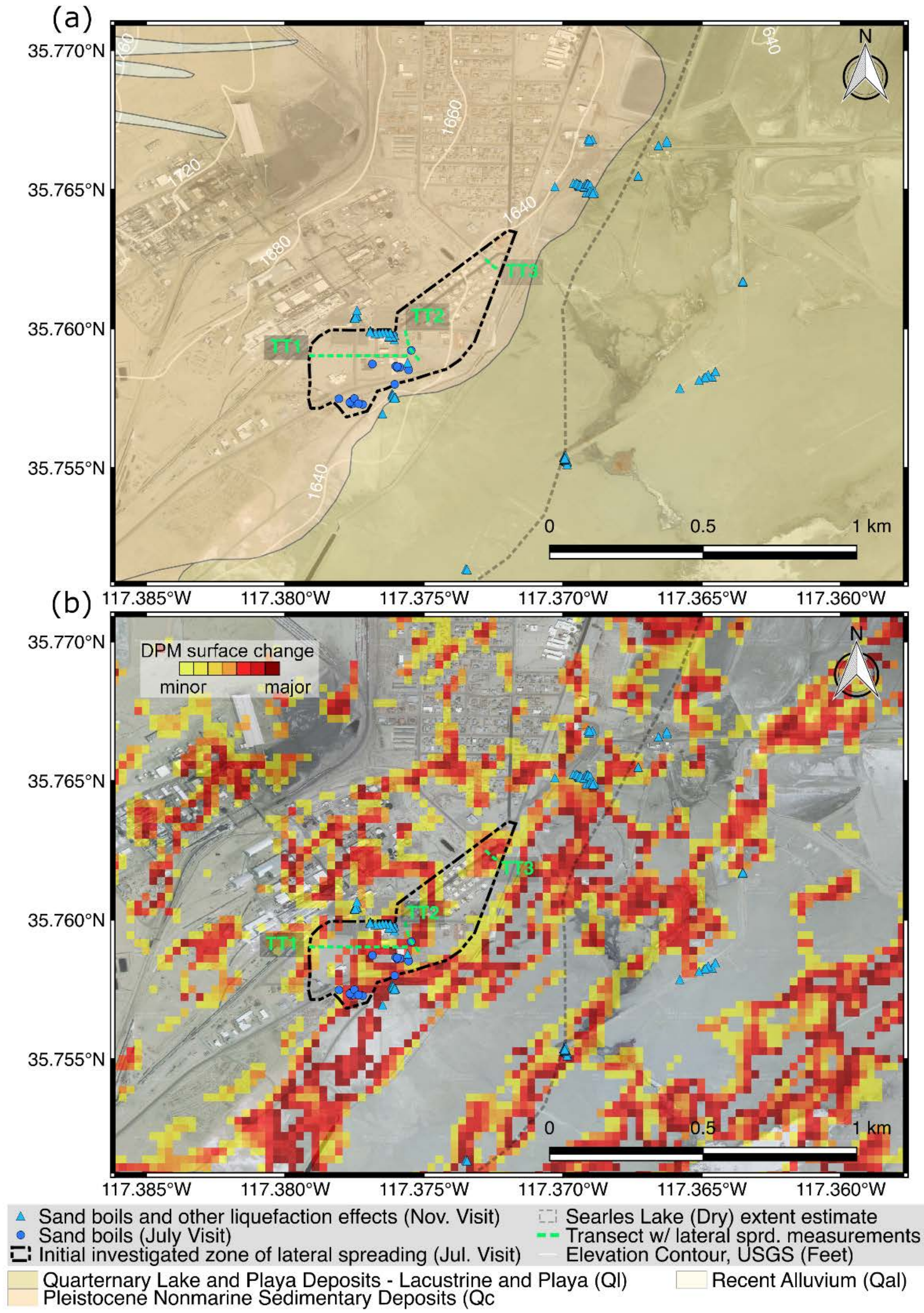

Figure 5. Map of Trona showing locations of observed liquefaction effects and lateral spreading measurement transects overlayed on (a) surface geology map and (b) damage proxy map. Geologic units are labeled following descriptions from Smith (2009).

Figure 6. Ground failure from liquefaction in Trona. (a) Sand boil along a pavement crack created from lateral spreading (35.757483°, -117.37806°). (b, c) Extensional cracks caused by lateral spreading (35.757325°, -117.377705°; 35.75966°, -117.375892°). (d, f) Damaged asphalt from buckled curb edge (35.75936°, -117.37676°; 35.762387°, -117.372586°). (e, h) Compressional features from lateral spreading (35.75897°, -117.37561°; 35.75909°, -117.37552°). (g) compressional and adjacent extensional

features/cracks caused by lateral spreading and ground oscillation (35.75986°, -117.37651°).

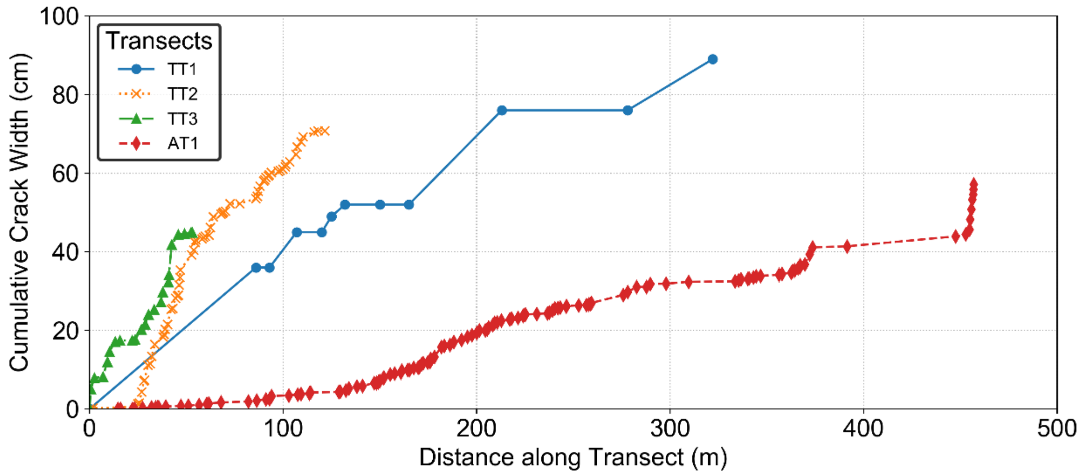

Figure 7. Cumulative crack width along transects in Trona and Argus. Transection locations are shown in Figures 4 and 7.

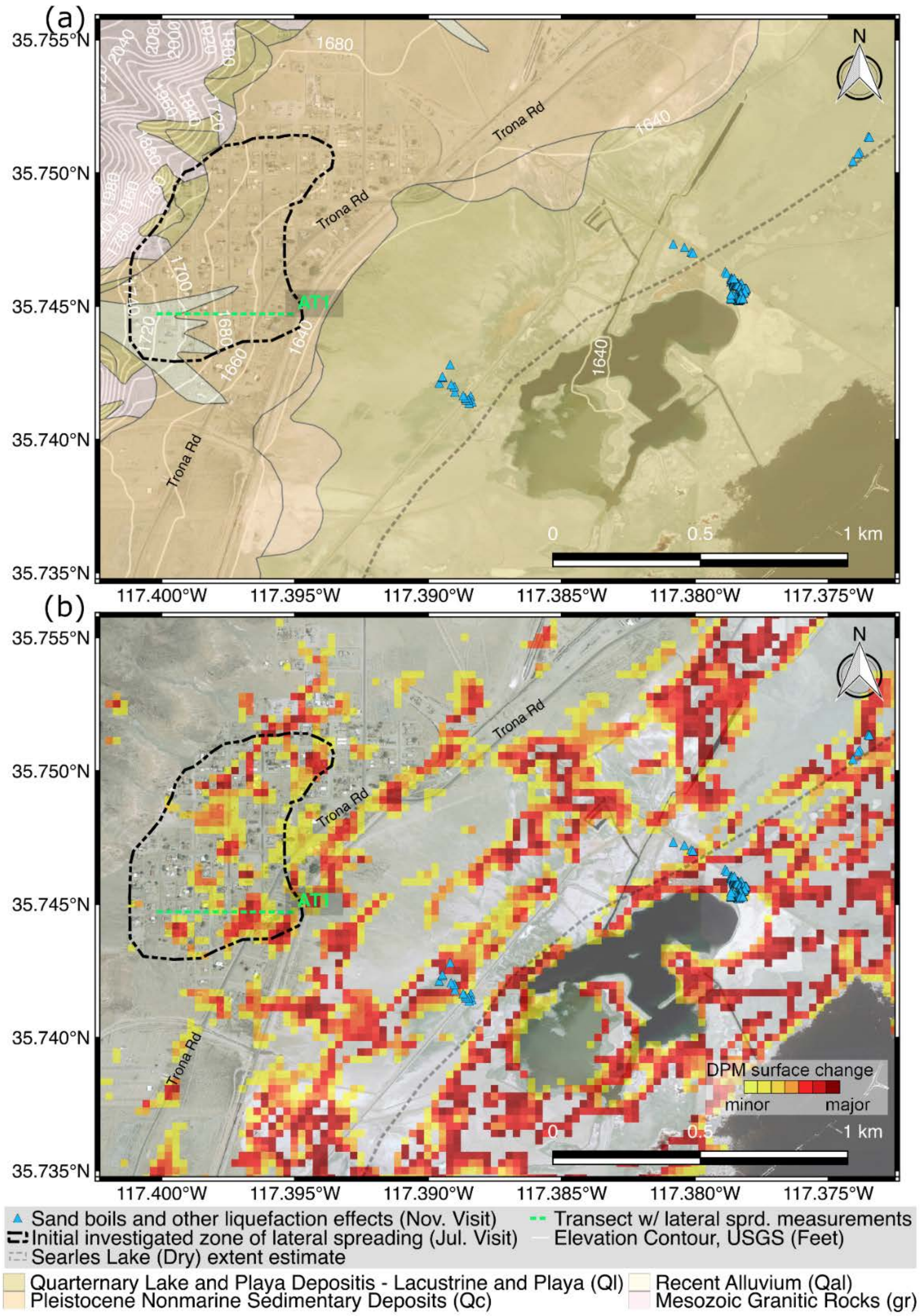

Figure 8. Map of Argus showing locations of observed liquefaction effects and lateral spreading measurement transects overlayed on (a) surface geology map and (b) damage proxy map. Geologic units are labeled following descriptions from Smith (2009).

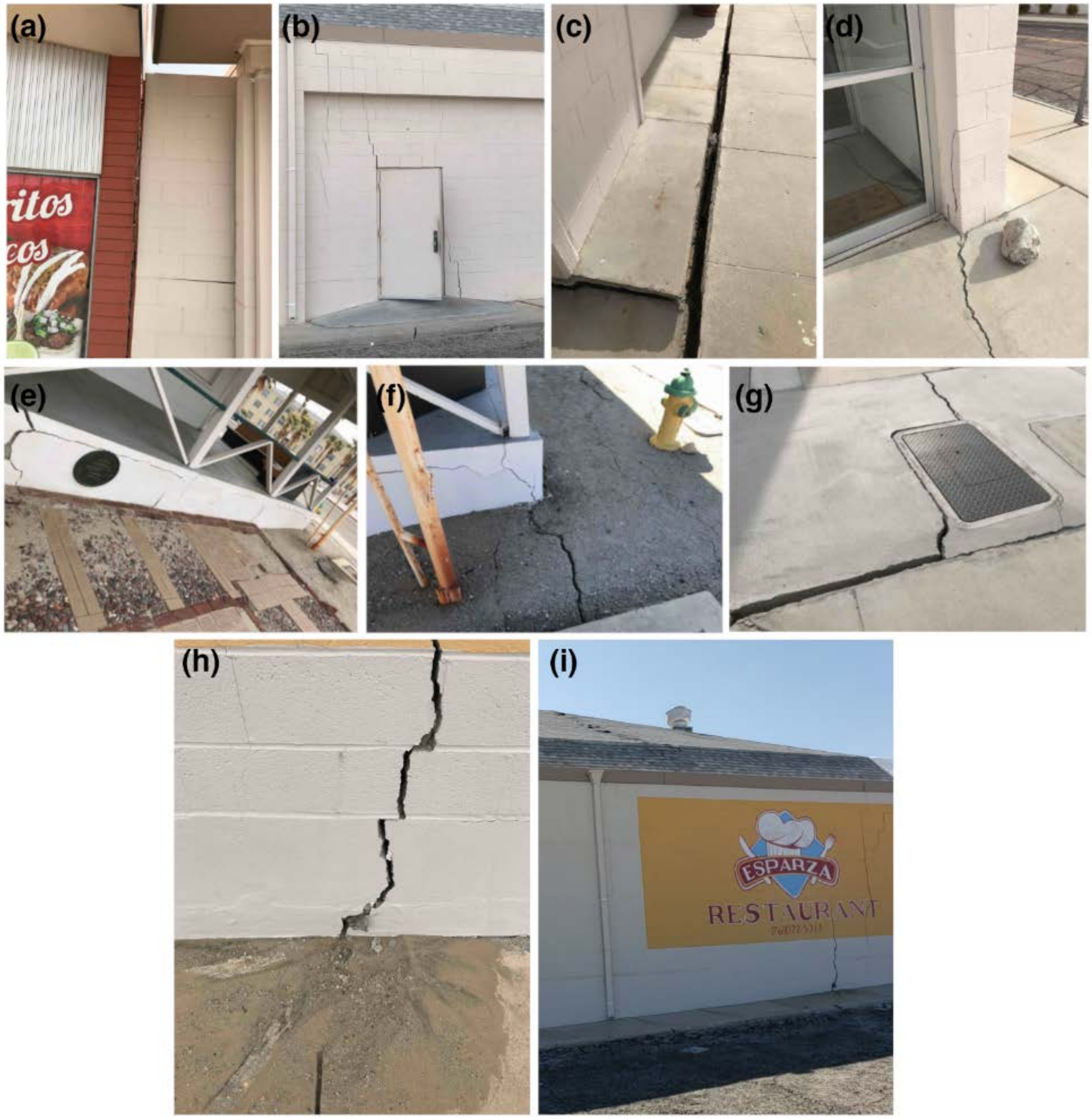

Figure 9. Ground failure effects on buildings in Trona. (a) Crack at screen wall between two buildings (35.75979°, -117.376315°). (b, h, i) Wall cracks at the eastern side of the Esparza restaurant with associated sand ejecta and roof damage (35.75957°, -117.37611°). (c, g) Sidewalk pavement crack and offset likely from lateral spreading and

ground oscillation (35.75982°, -117.37637°; 35.75980°, -117.37606°). (e, f) Cracks in floor slab from lateral spreading and ground oscillation (35.759802°, -117.376808°).

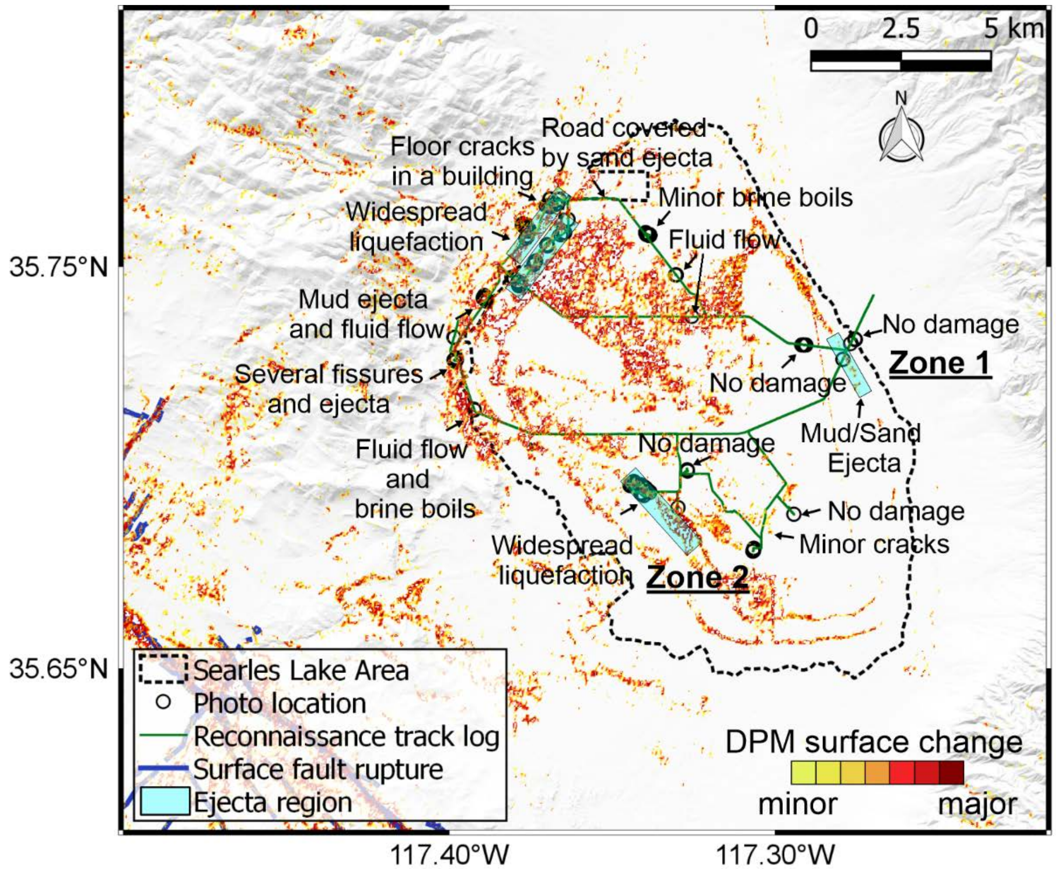

Figure 10. Damage proxy map produced following the **M**7.1 event, route of the November 2019 reconnaissance mission, geotagged photo locations, and reconnaissance findings.

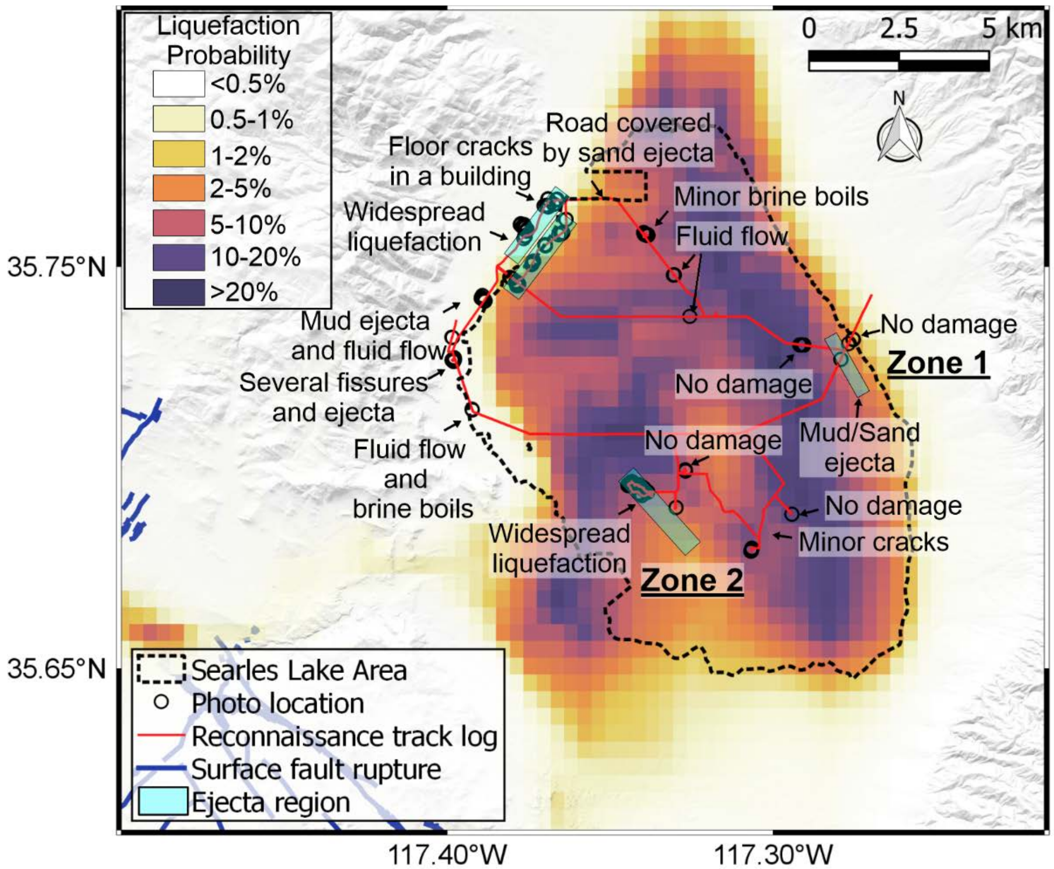

Figure 11. USGS liquefaction hazard map produced following the **M**7.1 event, route of the November 2019 reconnaissance mission, geotagged photo locations, and reconnaissance findings.

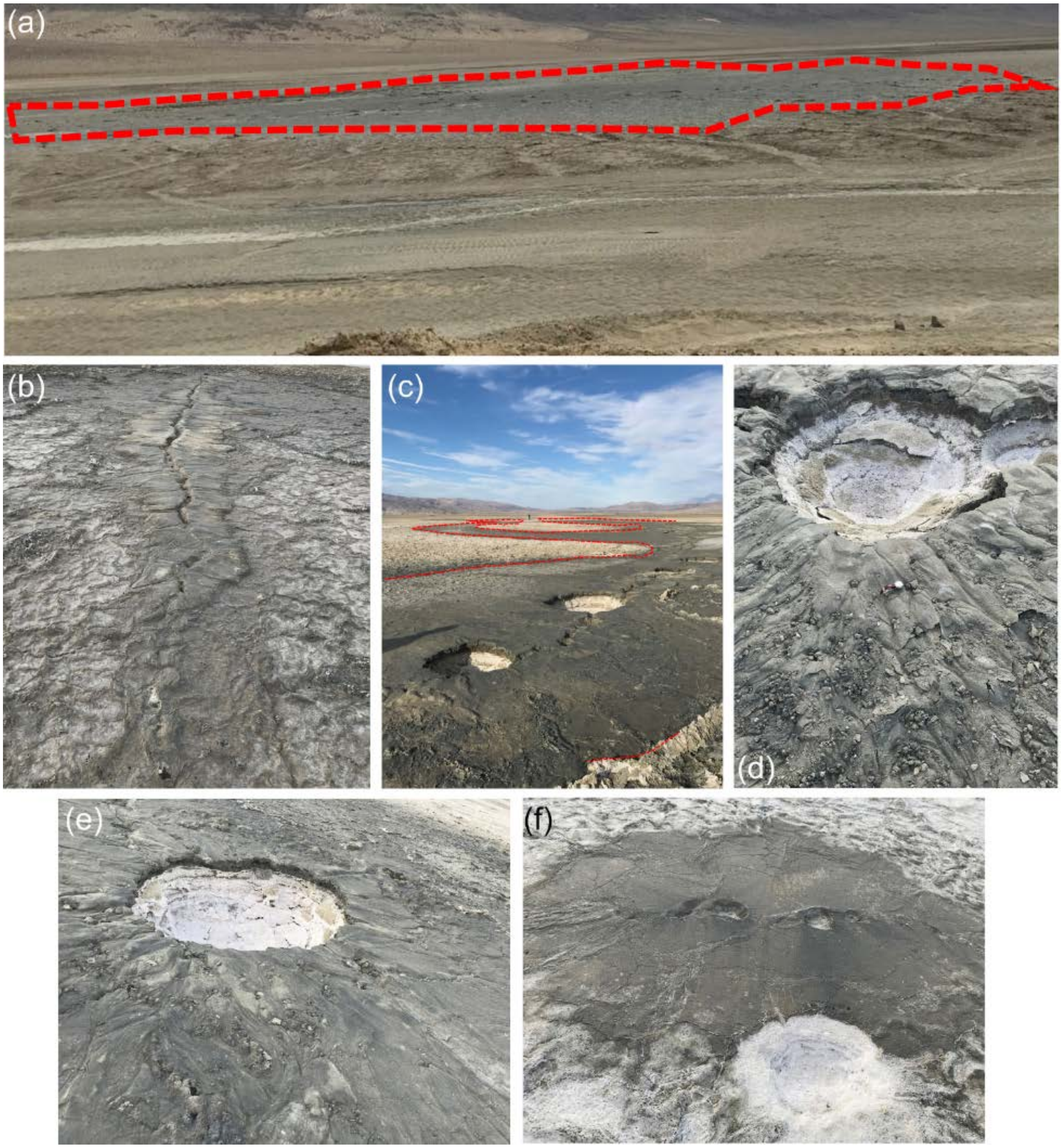

Figure 12. (a) Narrow liquefaction ejecta zone located in the central portion of the northeast edge of Searles Lake (35.72701°, -117.27801°), (b-f) fissures, sand boils with sand, gravel, and brine-evaporite ejecta observed towards the southwestern edge of the lake (35.694858°, -117.339622°; 35.6955°, -117.34235°; 35.695913°, -117.34113°; 35.695208°, -117.340462°; 35.695217°, -117.341072°).